Available on the CMS information server

CMS NOTE 2010/003

The Compact Muon Solenoid Experiment

CMS Note

Mailing address: CMS CERN, CH-1211 GENEVA 23, Switzerland

2010/03/02

Study of Various Photomultiplier Tubes with Muon Beams And Čerenkov Light Produced in Electron Showers

Yerevan Physics Institute, Yerevan, Armenia
S. Chatrchyan, V. Khachatryan, A.M. Sirunyan

National Centre for Particle and High Energy Physics, Minsk, Belarus
V. Mossolov, N. Shumeiko

Universiteit Antwerpen, Antwerpen, Belgium
E. A. De Wolf, S. Ochesanu, B. Roland, H. Van Haevermaet, P. Van Mechelen

Vrije Universiteit Brussel, Pleinlaan 2, 1050 Brussel, Belgium
Stijn Blyweert

Institute for Nuclear Research and Nuclear Energy, Sofia, Bulgaria
J. Damgov, L. Dimitrov, V. Genchev, S. Piperov, I. Vankov

E. Andronikashvili Institute of Physics, Academy of Science, Tbilisi, Georgia
V. Roinishvili

Deutsches Elektronen-Synchrotron, Hamburg, Germany
K. Borras, A. Campbell, H. Jung, I. Katkov, A. Knutsson, N. Sen

University of Athens, Athens, Greece
K. Panagiotis, A. Panagiotou[1], M. Theodoros

KFKI Research Institute for Particle and Nuclear Physics, Budapest, Hungary
A. Aranyi, G. Bencze[1], L. Boldizsar, D. Horvath[2], G. Vesztergombi

Panjab University, Chandigarh, India
S. Bansal, S.B. Beri, M. Jindal, M. Kaur, J.M. Kohli, M.Z. Mehta, N. Nishu, L.K. Saini, A. Singh, J.B. Singh

Tata Institute of Fundamental Research -EHEP, Mumbai, India
T. Aziz, A. Gurtu, M. Maity[3], D. Majumder, G. Majumder, K. Mazumdar, A. Saha, K. Sudhakar

Tata Institute of Fundamental Research -HECR, Mumbai, India
S. Banerjee, S. Dugad, N.K. Mondal

Institute for Studies in Theoretical Physics & Mathematics (IPM), Tehran, Iran
H. Arfaei, H. Bakhshiansohi, M. Mohammadi Najafabadi, S. Paktinat Mehdiabadi

INFN Sezione di Trieste , Universita di Trieste, Trieste, Italy
A. Penzo

Joint Institute for Nuclear Research, Dubna, Russia
P. Bunin, M. Finger, M. Finger Jr., I. Golutvin, V. Smirnov, A. Vishnevskiy, A. Volodko, A. Zarubin

Institute for Nuclear Research, Moscow, Russia
Y. Andreev, M. Kirsanov, A. Pashenkov, A. Toropin, S. Troitsky

Institute for Theoretical and Experimental Physics, Moscow, Russia
V. Epshteyn, V. Gavrilov, N. Ilina, V. Kaftanov* , M. Kossov[1], A. Krokhotin, S. Kuleshov, A. Oulianov, G. Safronov, S. Semenov, I. Shreyber, V. Stolin, E. Vlasov, A. Zhokin

Moscow State University, Moscow, Russia
A. Demianov, A. Ershov, A. Gribushin, V. Klyukhin, O. Kodolova, I. Lokhtin, S. Obraztsov, S. Petrushanko, A. Proskuryakov, L. Sarycheva, V. Savrin, I. Vardanyan

P.N. Lebedev Physical Institute, Moscow, Russia
I. Dremin, M. Kirakosyan, N. Konovalova, A. Vinogradov

State Research Center of Russian Federation, Institute for High Energy Physics, Protvino, Russia
V. Krychkine, V. Petrov, R. Ryutin, S. Slabospitsky, A. Sobol, A. Sytine, L. Tourtchanovitch, A. Volkov

Cukurova University, Adana, Turkey
A. Adiguzel, M.N. Bakirci, S. Cerci, I. Dumanoglu, E. Eskut, S. Girgis, E. Gurpinar, T. Karaman, A. Kayis Topaksu, P. Kurt, G. Onengut, K. Ozdemir, S. Ozturk, A. Polatoz, K. Sogut[4], B. Tali, H. Topakli, D. Uzun

Middle East Technical University, Physics Department, Ankara, Turkey
T. Aliev, M. Deniz, A.M. Guler, K. Ocalan, M. Serin, R. Sever, E. Yildirim, M. Zeyrek

Bogazici University, Department of Physics, Istanbul, Turkey
M. Deliomeroglu, E. Gulmez, A. Halu, B. Isildak, M. Kaya[5], O. Kaya[5], M. Ozbek, N. Sonmez[6]

National Scientific Center, Kharkov Institute of Physics and Technology, Kharkov, Ukraine
L. Levchuk, P. Sorokin

Boston University, Boston, USA
A. Clough, E. Hazen, A.H. Heering, A. Heister, J. St. John, P. Lawson, D. Lazic, J. Rohlf, L. Sulak, S. Wu

Brown University, Providence, USA
A. Avetisyan, J.P. Chou, S. Esen, G. Kukartsev, G. Landsberg, M. Narain, N. Nguyen, K.V. Tsang

University of California, Riverside, Riverside, USA
J.W. Gary, F. Liu, H. Nguyen, J. Sturdy

Fairfield University, Fairfield, USA
D. Winn

Fermi National Accelerator Laboratory, Batavia, USA
S. Banerjee, P.C. Bhat, M. Binkley*, F. Chlebana, I. Churin, S. Cihangir, M. Crawford, W. Dagenhart, M. Demarteau, G. Derylo, D. Dykstra, D.P. Eartly, J.E. Elias*, V.D. Elvira, J. Freeman, D. Green, A. Hahn, J. Hanlon, R.M. Harris, K. Kousouris, S. Kunori, P. Limon, C. Newman-Holmes, S. Sharma, W.J. Spalding, R. Vidal, J. Whitmore, W. Wu

Florida International University, Miami, USA
C. Ceron, V. Gaultney, L.M. Lebolo, S. Linn, P. Markowitz, G. Martinez

Florida State University, Tallahassee, USA
M. Bertoldi, S.V. Gleyzer, J. Haas, S. Hagopian, V. Hagopian, M. Jenkins, S. Sekmen

Florida Institute of Technology, Melbourne, USA
M.M. Baarmand, H. Mermerkaya, R. Ralich, I. Vodopiyanov

University of Illinois at Chicago (UIC), Chicago, USA
E.J. Garcia-Solis

The University of Iowa, Iowa City, USA
U. Akgun, E.A. Albayrak, B. Bilki, K. Cankocak[7], W. Clarida, F. Duru, E. McCliment, J.-P. Merlo, A. Mestvirishvili, A. Moeller, J. Nachtman, E. Norbeck, Y. Onel, F. Ozok, I. Schmidt, S. Sen, T. Yetkin, K. Yi

The University of Kansas, Lawrence, USA
O. Grachov, M. Murray, J.S. Wood

University of Maryland, College Park, USA
D. Baden, M. Boutemeur[8], S.C. Eno, D. Ferencek, N.J. Hadley, R.G. Kellogg, M. Kirn, K. Rossato, P. Rumerio, F. Santanastasio, A. Skuja, J. Temple, M.B. Tonjes, S.C. Ton-war, E. Twedt

University of Minnesota, Minneapolis, USA
P. Cole, P. Cushman, P.R. Dudero, K. Klapoetke, J. Mans

University of Mississippi, University, USA
L.M. Cremaldi, R. Godang, R. Kroeger, R. Rahmat, D.A. Sanders

Northwestern University, Evanston, USA
A. Anastassov, R.A. Ofierzynski, A. Pozdnyakov, M. Velasco, S. Won

University of Notre Dame, Notre Dame, USA
D.J. Karmgard, R. Ruchti, J. Warchol, J. Ziegler

Princeton University, Princeton, USA
N. Adam, E. Berry, D. Gerbaudo, V. Halyo, A. Hunt, J. Jones, E. Laird, D. Lopes Pegna, D. Marlow, T. Medvedeva, M. Mooney, J. Olsen, C. Tully, J.S. Werner, A. Zuranski

Purdue University, West Lafayette, USA
V.E. Barnes, A.T. Laasanen, A. Sedov

University of Rochester, Rochester, USA
A. Bodek, Y.S. Chung, P. de Barbaro, A. Garcia-Bellido, J. Han, A. Harel, D.C. Miner, D. Vishnevskiy, M. Zielinski

The Rockefeller University, New York, USA
A. Bhatti, K. Goulianos, M. Yan

Texas A&M University, College Station, USA
A. Gurrola, T. Kamon, S. Sengupta, D. Toback, M. Weinberger

Texas Tech University, Lubbock, USA
N. Akchurin, C. Jeong, S.W. Lee, S. Popescu, Y. Roh, A. Sill, I. Volobouev, R. Wigmans, E. Yazgan

Abstract

The PMTs of the CMS Hadron Forward calorimeter were found to generate a large size signal when their windows were traversed by energetic charged particles. This signal, which is due to Čerenkov light production at the PMT window, could interfere with the calorimeter signal and mislead the measurements. In order to find a viable solution to this problem, the response of four different types of PMTs to muons traversing their windows at different orientations is measured at the H2 beam-line at CERN. Certain kinds of PMTs with thinner windows show significantly lower response to direct muon incidence. For the four anode PMT, a simple and powerful algorithm to identify such events and recover the PMT signal using the signals of the quadrants without window hits is also presented. For the measurement of PMT responses to Čerenkov light, the Hadron Forward calorimeter signal was mimicked by two different setups in electron beams and the PMT performances were compared with each other. Superior performance of particular PMTs was observed.

---

[*] Deceased

[1] Also at CERN, European Organization for Nuclear Research, Geneva, Switzerland

[2] Also at Institute of Nuclear Research ATOMKI, Debrecen, Hungary

[3] Also at University of Visva-Bharati, Santiniketan, India

[4] Also at Mersin University, Mersin, Turkey

[5] Also at Kafkas University, Kars, Turkey

[6] Also at Ege University, Izmir, Turkey

[7] Also at Istanbul Technical University, Istanbul, Turkey

[8] Also at University of Savoie, Polytech Annecy, France

Corresponding author: Burak Bilki (Burak.Bilki@cern.ch)

1 Introduction

The Compact Muon Solenoid (CMS) [1] is a general-purpose detector designed to run at the highest luminosity provided by the CERN Large Hadron Collider (LHC). Coverage between pseudorapidities of 3.0 and 5.0 is provided by the steel/quartz fiber Hadron Forward (HF) calorimeter. The front face is located at 11.2 m from the interaction point and the depth of the absorber is 1.65 m. The signal originates from Čerenkov light emitted in the quartz fibers, which is then channeled by the fibers to photomultipliers. The absorber structure is created by machining 1 mm square grooves into steel plates, which are then diffusion welded. The diameter of the quartz fibers is 0.6 mm and they are placed 5 mm apart in a square grid. The quartz fibers, which run parallel to the beamline, have two different lengths (1.43 m and 1.65 m) which are inserted into grooves, creating two effective longitudinal samplings. There are 13 towers in η, all with a size given by $\Delta\eta \approx 0.175$, except for the lowest-η tower with $\Delta\eta \approx 0.1$ and the highest-η tower with $\Delta\eta \approx 0.3$. The ϕ segmentation of all towers is 10°, except for the highest-η one which has $\Delta\phi = 20^\circ$. This leads to 900 towers and 1800 channels in the two HF modules [2]. Details of the HF design, together with test beam results and calibration methods, can be found in [3].

In the framework of the Super LHC (SLHC) upgrade plans, one of the problems to be solved is the large signal generated by the photomultiplier tubes (PMTs) of CMS HF calorimeters when the PMT window is traversed by relativistic charged particles. The primary reason for this signal is Čerenkov light production at the PMT window, followed by the liberation of photoelectrons at the photocathode of the PMT.

There have been a few studies to tag these events such as using a scintillating crystal in front of the PMT window to enhance the light production by the traversing particle while keeping the light sensitivity of the PMT practically constant, utilizing a much smaller diameter round PMT with a thinner window to reduce the rate of such events and using a veto counter possibly behind the readout box.

In this study, we compare different types of candidate PMTs with the currently installed PMT (hereon called HFPMT) for signal production at PMT window with the muon beam and for Čerenkov light detection with two different setups in electron showers. A simple and efficient tagging and signal recovery algorithm for the PMT window events of the four anode PMT is also discussed.

2 Experimental Setup and Data Acquisition

Table 1 summarizes typical properties of the PMTs used in this study. Three different kinds of four anode PMTs (R7600U-100-M4, R7600U-200-M4 and R8900U-100-M4), two kinds of single anode PMTs (R7600U-100 and R7600U-200) and miniPMT (R9880U-110) were tested for comparison with each other and the currently installed HFPMT (R7525). The candidate PMTs offer superior performance over HFPMT due to their increased quantum efficiencies. Their geometrical specifications predict a significant reduction in both rate and the amount of signal generation when the PMT window is hit by a charged particle (HFPMT window is 2 mm thick at the center and

gets thicker towards the rim, single and four anode PMT windows are slightly less than 1 mm thick and miniPMT window is around 0.5 mm thick).

Table 1: Typical properties of PMTs tested in this study. Information is obtained from Hamamatsu [4]. Detailed information about the HFPMT can be found in [5].

PMT Type	PMT Type Number	Photocathode	Quantum Efficiency (max. %)	Typical Gain	Window Area (mm^2) app.
Four Anode PMT	R7600U-100-M4	Super Bialkali	35	1.3×10^6	324 (square)
Four Anode PMT	R7600U-200-M4	Ultra Bialkali	43	1.3×10^6	324 (square)
Four Anode PMT	R8900U-100-M4	Super Bialkali	35	1.0×10^6	324 (square)
Single Anode PMT	R7600U-100	Super Bialkali	35	1.0×10^6	324 (square)
Single Anode PMT	R7600U-200	Ultra Bialkali	43	1.0×10^6	324 (square)
miniPMT	R9880U-110	Super Bialkali	40	2.0×10^6	50 (round)
HFPMT	R7525	Bialkali	25	5.0×10^5	490 (round)

The PMTs were tested with 150 GeV/c muon beam and 80 GeV/c electron beam of CERN H2 beam-line [6] in July 2009.

As one of the four main test stations on the HF test table, two different setups were used to test the muon response of the PMTs. In the first setup (Fig. 1a), PMTs were lined one after the other with their windows facing the same direction. In the second setup (Fig. 1b), PMTs were placed side by side, again with their windows facing the same direction. The first setup was used to study the PMT response when the muon beam hits the PMT windows from the front and the second setup was used to investigate the response when the beam hits sideways. Both PMT boxes were made light-tight and they were placed in front of wire chamber E (WCE) as the first test apparatus on the HF test table in order to perform precise position measurements with 1 mm resolution.

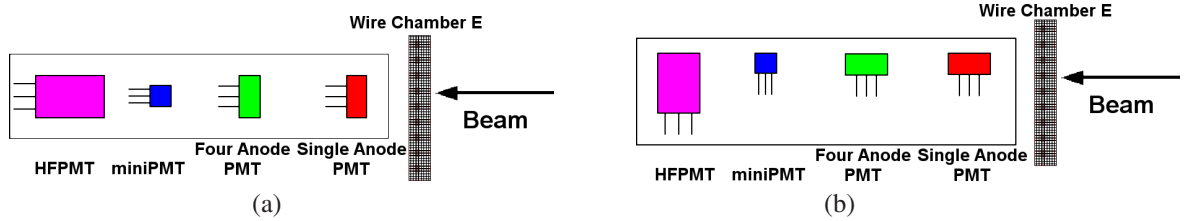

Figure 1: Sample layout of the PMT Box for front (a) and side (b) muon incidence. PMT bases are indicated by three parallel lines (not to scale).

Two test stations were used to measure the differences in the response of the PMTs to Čerenkov light from electron showers (Fig. 2). During the electron shower tests, a 5 cm thick steel absorber is introduced upstream in order to instantiate the electromagnetic shower and produce a reasonable amount of Čerenkov light for the two PMTs attached to the end of the HF fiber bundle. The $\sim$1 cm diameter bundle of regular HF quartz fibers (with 0.6 mm diameter) was placed in $\sim$3 cm diameter light guide. The bundle splits into two parts at the readout end. The HFPMT was kept in place at one end of the fiber bundle while the candidate PMTs were interchanged at the other end. The possible signal difference between the two ends due to fiber mixing was also measured. The portion of

the fiber bundle that sees the beam was aligned to make ∼45° with respect to the beam direction. The length of the bundle from the beam interaction to readout was ∼1.5 m. WCE was used to select events with electrons that pass through the fiber bundle.

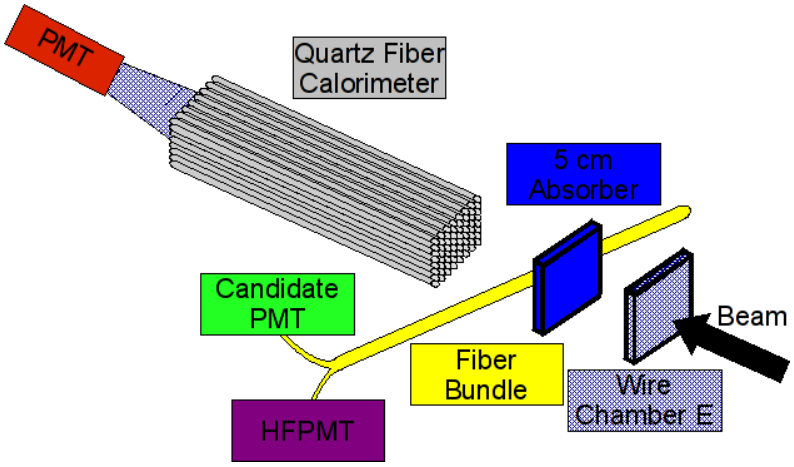

Figure 2: Quartz fiber calorimeter and fiber bundle test setups (not to scale).

The second test station for the electron showers was the quartz fiber calorimeter. It consisted of an array of 6 mm diameter, 45 cm long steel rods in a 20 cm x 20 cm x 45 cm housing with quartz fibers (0.3 mm core diameter, 65 cm long) inserted in between the rods. The fibers were then bundled at the back of the calorimeter to form a single readout. The light guides at the readout end were 20 cm long with the same reflective material as HF light guide.

The readout was performed by charge integration and encoding units (QIEs) [7] and the data was stored in CMSSW (CMS SoftWare) [8] HCAL Test Beam raw data format. Each QIE channel was readout in 20 time slices of 25 ns length each. A schematic of the end of H2 beam-line is shown in Fig. 3. The trigger was given by the coincidence of two scintillation counters of sizes 14 cm x 14 cm (SC1) and 4 cm x 4 cm (SC2). Therefore, a beam spot of size 4 cm x 4 cm is anticipated. However, for some of the muon runs, HCAL beam test wedge was in front of the HF test table, and for these runs a beam spot of at least 10 cm x 10 cm was recorded by WCE due to multiple scattering of muons off the wedge. For some of the muon runs, wire chamber D (WCD) was also utilized to track and veto muons with a high deviation from the original beam direction. It was verified that this did not affect the results significantly since the PMT window size is small compared to the size of the wire chambers.

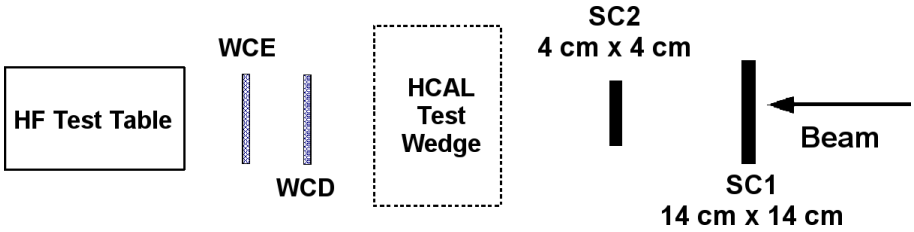

Figure 3: Schematic of the end of H2 beam-line (not to scale) showing scintillation counters (SC1 and SC2) and wire chambers D and E (WCD and WCE) together with the HF test table and the HCAL test wedge that was in the beam-line for some of the runs.

3 Testing Muon Interactions with PMT Windows

3.1 PMT Response to Front Muon Incidence

The setup shown in Fig. 1a was exposed to muon beams both with/without the HCAL test wedge in front. The results were compared and it was verified that the wire chamber utilization was satisfactory for the selection of events in the region of interest. Figure 4 shows the QIE charge profile as a function of wire chamber coordinates for the HFPMT. Similar results were obtained for all types of PMTs tested. Using these profiles, a position cut with the correct dimensions at the PMT window edges was applied to study only the events where the charged particles traversed the PMT windows. The cut for the HFPMT window is shown in Fig. 4.

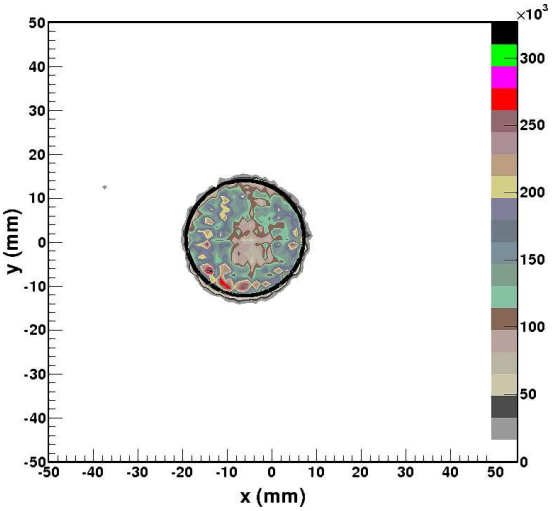

Figure 4: Integrated charge profile as a function of WCE coordinates for HFPMT. The boundary of the PMT window event selection is shown as a black ring.

Figure 5 shows the responses of different types of PMTs when the muon beam hits the PMT window from the front. All responses are normalized to the gain of the HFPMT. The charge for the four anode PMT was calculated by adding the signals from the four channels that read out the four quadrants of the PMT window after individual gain normalizations. Since HFPMT window is much thicker than that of the other PMTs, Čerenkov signal produced is much higher. It has a signal magnitude that is more than a factor of two compared to the single anode and four anode PMTs and a much larger spread with a long tail in the high end of the spectrum. The four anode and single anode PMTs both have ultra bialkali photocathodes and they exhibit the same behavior in the overall picture. The miniPMT window produces the lowest magnitude of signal among all because of its tiny window thickness and the response shows no tail in the larger signal region. However, the width of the distribution is not improved as much.

With the PMT window cuts applied, PMT window event rates were also measured as the ratio of the number of events above pedestal to the total number of events: HFPMT 90%, four anode PMT 69%, single anode PMT 64% and miniPMT 51%. As expected, the window event rates were found to be correlated with the thicknesses of the PMT windows.

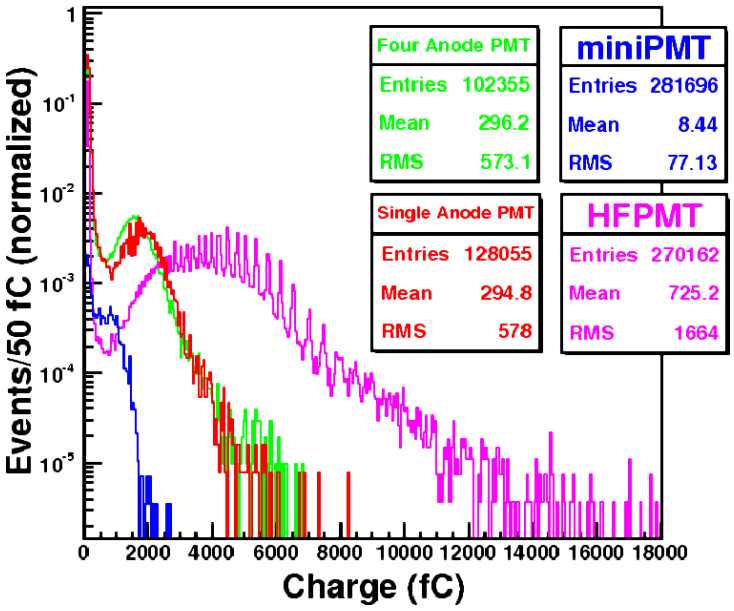

Figure 5: Charge distributions of the four anode PMT (R7600U-200-M4), the single anode PMT (R7600U-200), the miniPMT and the HFPMT produced by the front beam incidence.

3.2 PMT Response to Side Muon Incidence

The responses of three PMTs with different window geometries for side beam incidence (Fig. 1b) are shown in Fig. 6a. These distributions were obtained after carefully applying a position cut on the PMT window. An example of such a cut is shown in Fig. 6b. The pulse amplitudes are 2-5 times larger when compared to the case where the beam hits the PMT window from the front as the distance the particle travels inside the PMT window is much longer for side incidence. Since the window thickness seen by the beam is not uniform for the HFPMT and the miniPMT, the distributions of these PMTs are suppressed towards lower values of charge. Single anode PMT exhibits identical behavior as the four anode PMT, therefore its charge distribution was not shown in Fig. 6a.

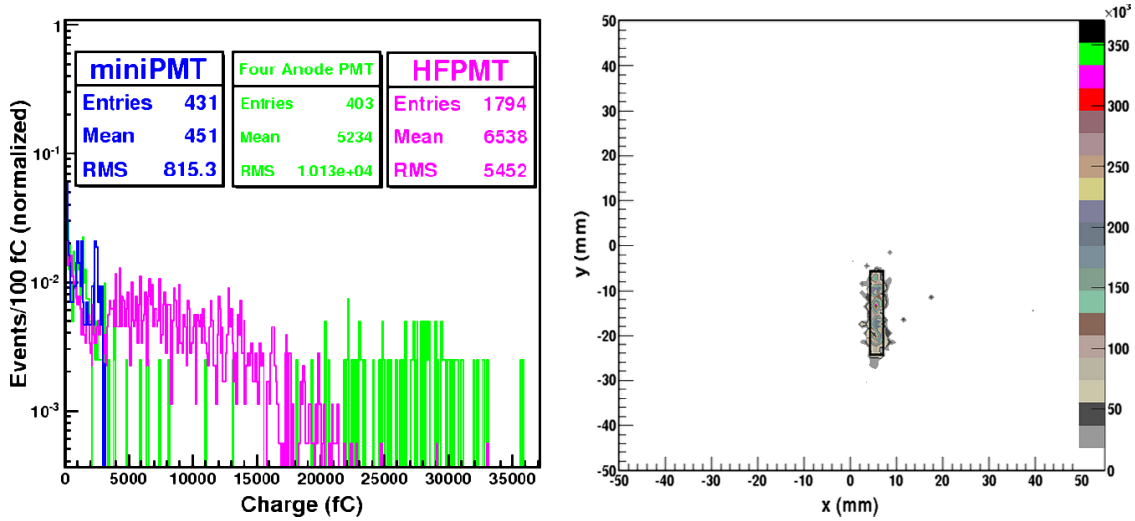

(a) (b)

Figure 6: (a) Charge distributions of the four anode PMT, the miniPMT and the HFPMT as produced by the side beam incidence. (b) Charge profile and selection region for four anode PMT (R8900U-100-M4).

3.3 Angular Study of Muon Incidence on Four Anode PMT

One of the four anode PMTs (R8900U-100-M4) was used to study the dependence of the charge distribution on the angle of incidence of the beam. The PMT was exposed to beam with its window making an angle of 90° (front incidence), 70°, 50°, 30°, 10° and 0° (side incidence) with respect to the beam direction. Beam position cuts were applied around the PMT window using WCE information for each orientation. Figure 7a shows the charge distributions for 50°, 10° and 0°. As the angle is reduced from 90°, the length of the PMT window that is exposed to beam increases leading to an increase in signal magnitude (Fig. 7b). The results of the angular study are consistent with the results presented in [9] for bialkali photocathodes.

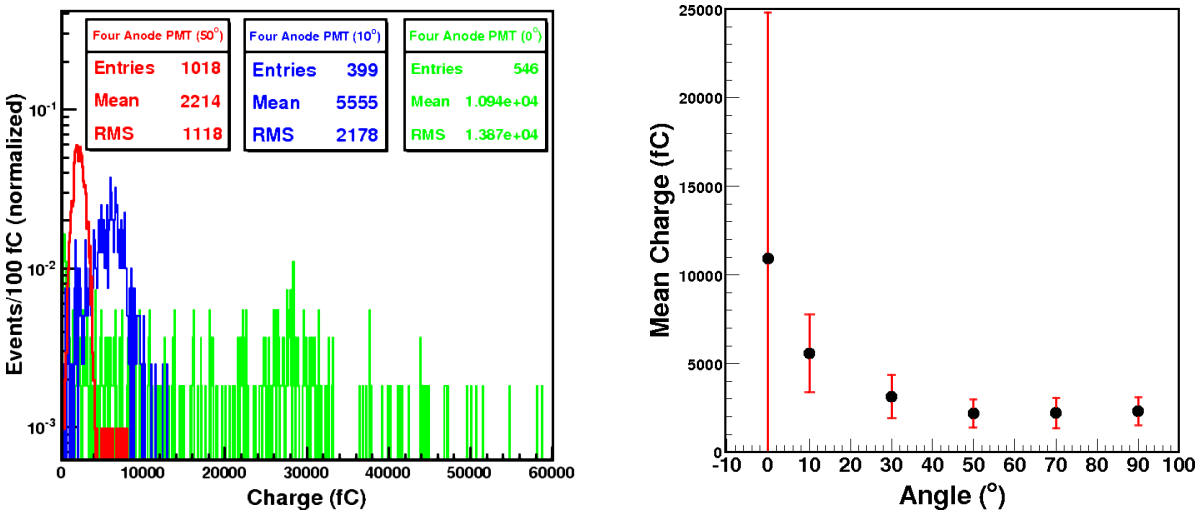

(a) (b)

Figure 7: (a) Charge distribution of the four anode PMT (R8900U-100-M4) for different angles of muon beam incidence. (b) Mean charge at all angles studied.

4 Testing Čerenkov Response of PMTs

4.1 Tests with the Fiber Bundle

The setup is prepared by first introducing a 5 cm thick steel absorber in front of the fiber bundle (see Fig. 2). The bundle sees the beam at 45° angle. Čerenkov light produced in the section of the fiber bundle that is exposed to the initial electron shower propagates to the end where the bundle splits into two light guides. Figure 8 shows the charge distributions measured by a four anode PMT when it was reading out from the two ends of the fiber bundle one at a time. The distributions prove that the mixing of the fibers is satisfactory enough so that both ends could be treated as identical for the purpose of testing two different types of PMTs at once.

The fiber bundle was visualized using PMT charge profile for WCE coordinates. Since the actual bundle was about 1 cm in diameter, a cut on the wire chamber coordinates was applied to insure the measurement of the signal coming only from the Čerenkov light production in the fiber bundle. Figure 9 shows the profile for the four anode

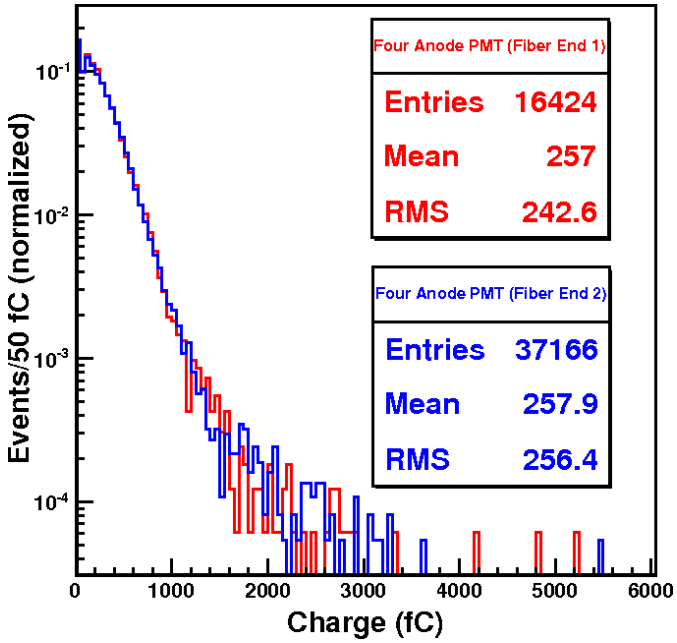

Figure 8: Charge distributions for a four anode PMT when it was reading out different ends of the fiber bundle while all other parameters in the setup were kept constant.

PMT. The bundle is along the horizontal direction. The size of the cut was kept slightly less than the actual size of the fiber that is exposed to beam. Due to the small ratio of the selection area to the size of the beam and the moderate efficiency of the wire chamber, the number of selected events were about 20% of the total number of events recorded.

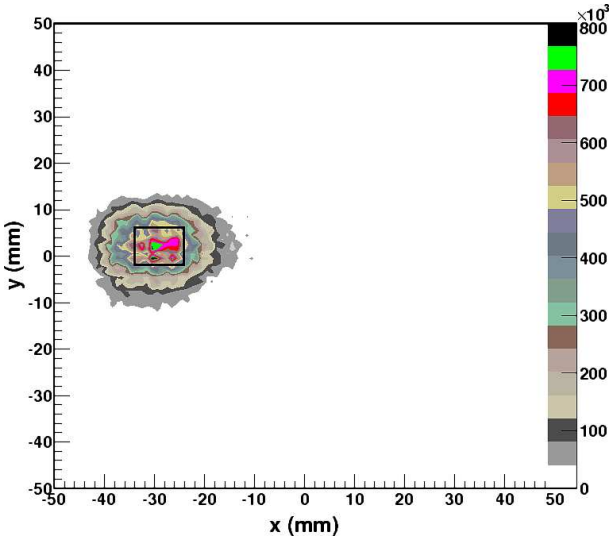

Figure 9: Integrated charge profile as a function of WCE coordinates for a four anode PMT (R7600U-100-M4). Black rectangle shows the selection cut applied in order to include the signal from the fiber bundle only.

Figure 10 shows the charge distributions for the PMTs reading out the fiber bundle signal. The distributions were normalized to the HFPMT gain. Single anode and four anode PMT signals both have a mean $\sim$1.5 times the HFPMT signal. The single anode PMT is of type R7600U-100 and the four anode PMT is of type R7600U-100-

M4 both with super bialkali photocathodes. Hence their signals are comparable. Also shown are the Gaussian fits to the data. All distributions are well described by the fits. Deviations from the fit are mainly due to the fluctuations in the charge integration and encoding system.

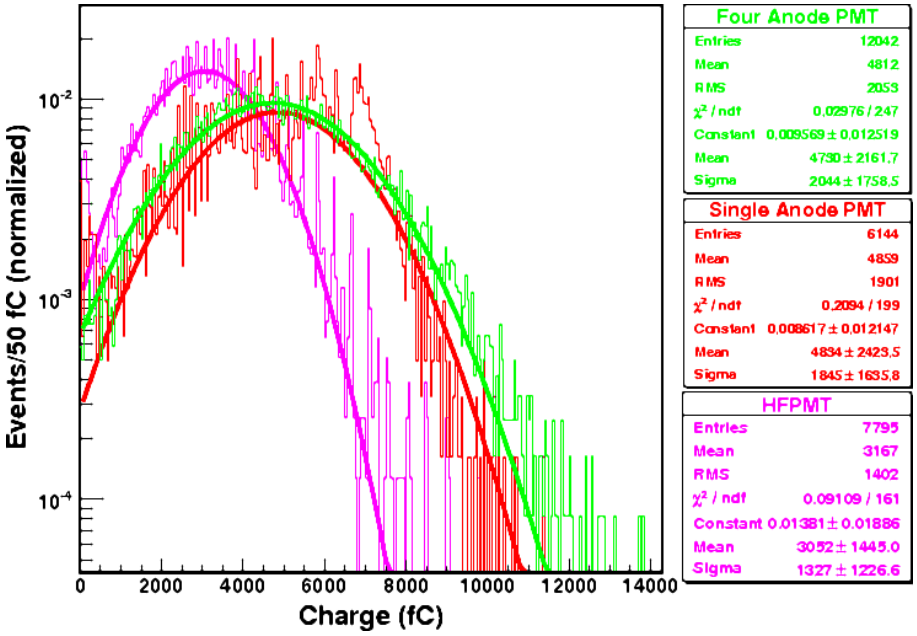

Figure 10: Fiber bundle charge distributions for the four anode PMT (R7600U-100-M4), the single anode PMT (R7600U-100) and the HFPMT. Gaussian fits are also shown.

4.2 Tests with the Quartz Fiber Calorimeter

The fiber calorimeter was placed behind the 5 cm thick steel absorber. The calorimeter was positioned so that the fibers were aligned along the beam direction and were bundled at the back of the calorimeter (see Fig. 2). Therefore, 80 GeV/c electrons reach the fiber calorimeter as a developing shower that reaches its maximum within the first quarter length of the calorimeter and the electromagnetic shower would be contained entirely. No cuts on the particle position are applied as the main testing point is to obtain a sufficient amount of signal by collecting maximum Čerenkov light out of the calorimeter fibers.

The charge distributions of the four anode PMT (R7600U-200-M4), the single anode PMT (R7600U-200), the miniPMT and the HFPMT are shown in Fig. 11. The four anode PMT and the single anode PMT with ultra bialkali photocathodes read about twice the magnitude of the signal collected by the HFPMT. The distributions were normalized to the HFPMT gain. No PMT window area corrections were applied since proper light guides were utilized for each PMT window geometry. The miniPMT window area is smaller than the bundle cross-section area, hence its charge distibution is presented only to show that more than one miniPMT per readout channel for HF calorimeter would be necessary.

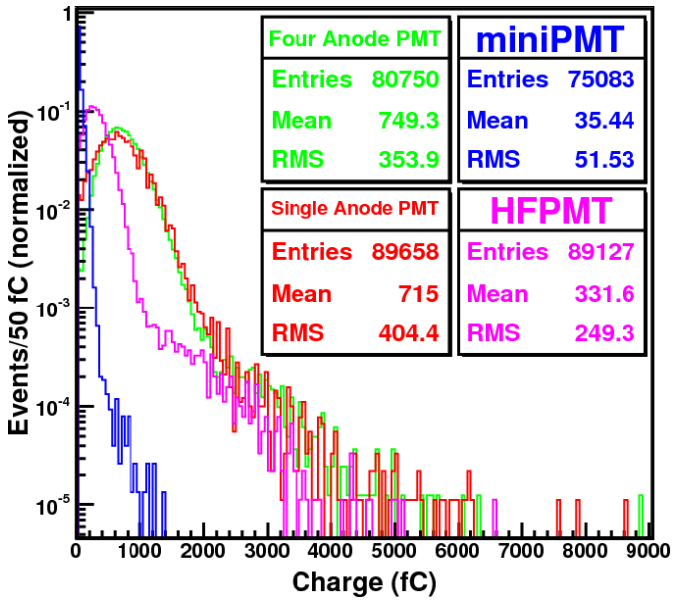

Figure 11: Quartz fiber calorimeter charge distributions for four anode PMT (R7600U-200-M4), single anode PMT (R7600U-200), miniPMT and HFPMT.

5 Selecting PMT Window Events and Recovering the Signal with Four Anode PMT

A simple algorithm for identifying window events in the four anode PMTs has been developed with the assumption of using them in HF. The signal from the HF fibers should be shared almost equally by the four channels while the window event signal emerges as a large deviation of one or more quadrant signal from the average signal of the four quadrants. Figure 12 shows the distribution of the maximum deviation of any quadrant signal from the mean signal of the four quadrants both for a window event sample and an electron shower sample with the HF fiber bundle. The deviation for a real signal is within one mean whereas for the PMT window events, the deviation of a single quadrant signal extends up to three times the average signal. The cut to distinguish the PMT window events from the real signal is set at a maximum deviation of one mean from the average. This introduces a systematic error of about 5% in the cut algorithm.

Once the PMT window event is identified, the PMT signal is recovered by averaging the signals from the quadrants that do not show window event signature and multiplying that number by four. The single quadrant PMT window event signature is determined as the ratio of the two highest signals being greater than 20. Although this case constitutes the majority of all the window events (about 80%), there is also multiple quadrant hit signatures in front muon incidence. When the muon hit is close to the center of the PMT window, the produced Čerenkov light is shared (usually unequally) by the neighbor quadrants. This phenomenon can not be considered as crosstalk between the quadrants since the light incidence on the photocathode is not point-like. Rather, it is about 1.3 mm diameter disc of Čerenkov light on the photocathode. The fraction of such events is around 2.5%. This is consistent with the ratio of the central area to the whole PMT window area (around 2.3%). Further selection is applied in

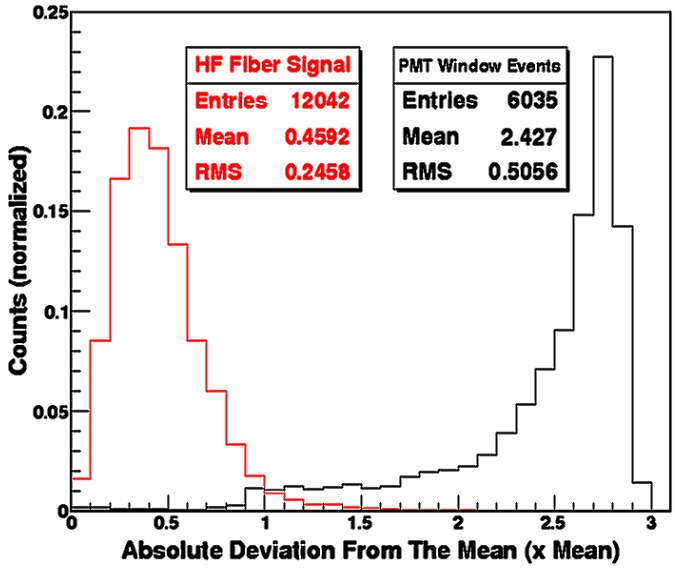

Figure 12: The distributions of maximum absolute deviation of single quadrant signal from the average signal of the four quadrants as multiples of mean signal (red: Čerenkov signal; black: PMT window event signal).

order to reduce this effect: If one of the three quadrants have more than 80% of the total signal (of the three), the event is assigned the double quadrant hit signature. The recovery is performed using the two quadrants with the lowest signals. The recovered signal for the remaining negligible fraction of events is calculated by multiplying the smallest signal by four.

Figure 13 shows the application of this PMT window event identification and signal recovery algorithm to a set of front muon incidence data. No pedestal subtraction has been applied to the data. The algorithm successfully selects the PMT window events and recovers the signal back. The distribution is suppressed towards zero, slightly above pedestal - which is shown by the blue, crossed distribution - except for the events with muon hits around the center of the PMT window which correspond to $\sim$2.5% of all the front-incident muon events.

Figure 14 shows the results of the same algorithm applied to the side incidence data. PMT window events are selected and the signal is recovered with more than 95% efficiency. Events with muons that pass through the center of the four anode PMT generate a high signal in all four quadrants, but the rate of such events is below 1% which is consistent with the fraction of the central boundary area seen sideways (1.1%). Similar results are obtained for all different angles that were tested. The algorithm is an efficient way of tagging and correcting for cosmic events.

The algorithm was also applied to the data from the HF fiber bundle. The result is shown in Fig. 15. The method is applied with no pedestal subtraction or gain normalization. The algorithm misidentifies about 6% of the signal events as PMT window events and reconstructs the signal suppressing it towards zero. The misidentification is due to the algorithm itself; however, the suppression towards zero is due to slight alignment variations that result in uneven illumination of the quadrants or real interference from particles scattered towards the four anode PMT or cosmic muons.

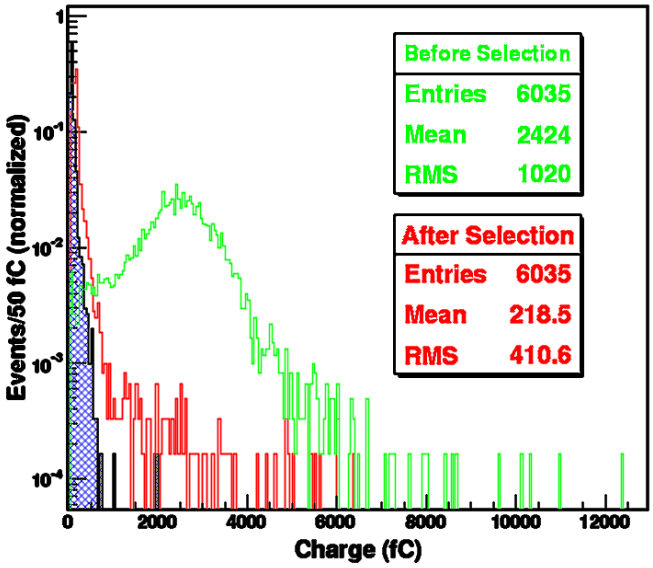

Figure 13: PMT window event selection and signal recovery for the four anode PMT with front incidence of muons. No pedestal subtraction was applied to the data. The blue, crossed area is the pedestal.

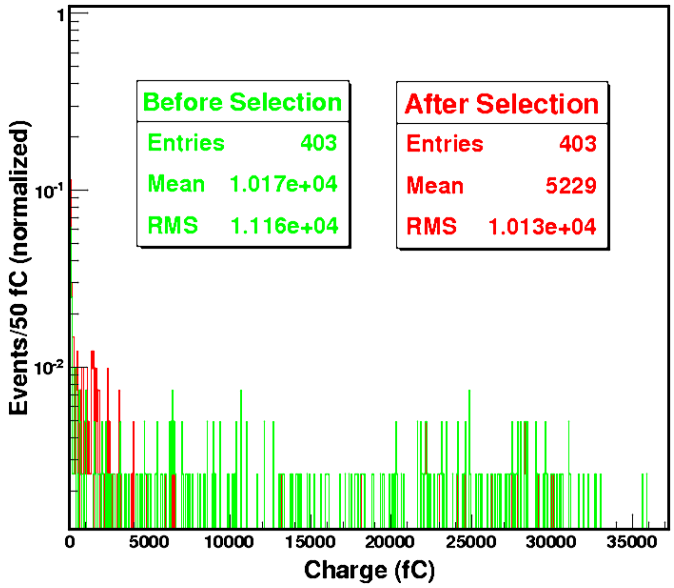

Figure 14: PMT window event selection and signal recovery for the four anode PMT with muons at side incidence. No pedestal subtraction was applied to the data.

For some of the runs, the fiber calorimeter was rotated by 60° or 90° to allow the electron shower to leak behind, and the fiber bundle PMTs were placed in the beamline at the back of the calorimeter. Although the probability for the PMTs to get real particle hits together with the bundle signal is too low, the algorithm was tested with this setup for its effectiveness in selecting PMT window events within a real signal. The result is shown in Fig. 16. In the low signal region of the spectrum, the signal is suppressed towards zero as in the case of the algorithm applied to pure signal. However, in the mid- to high-signal regions of the spectrum, the signal is suppressed towards slightly lower values indicating that efficient identification and signal recovery has been performed. The most important

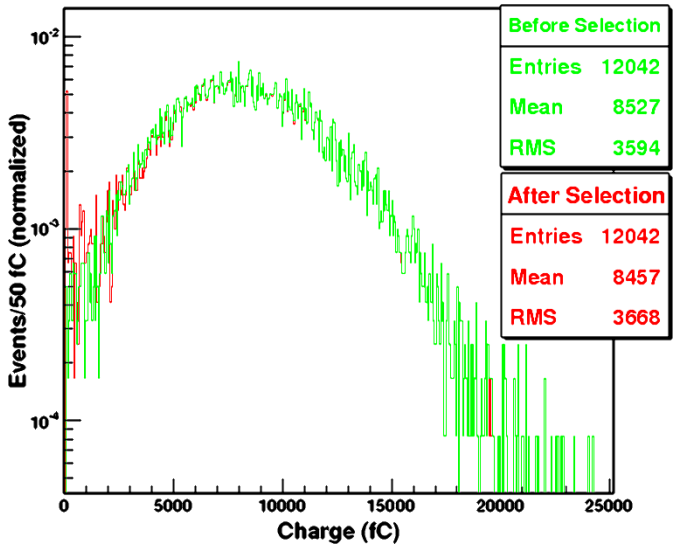

Figure 15: Charge distributions before and after the algorithm for selection of PMT window events and signal recovery was applied to the four anode PMT of the HF fiber bundle.

aspect of this result is that the high tail in the original distribution, which clearly comes from PMT window events, disappears after the utilization of the algorithm.

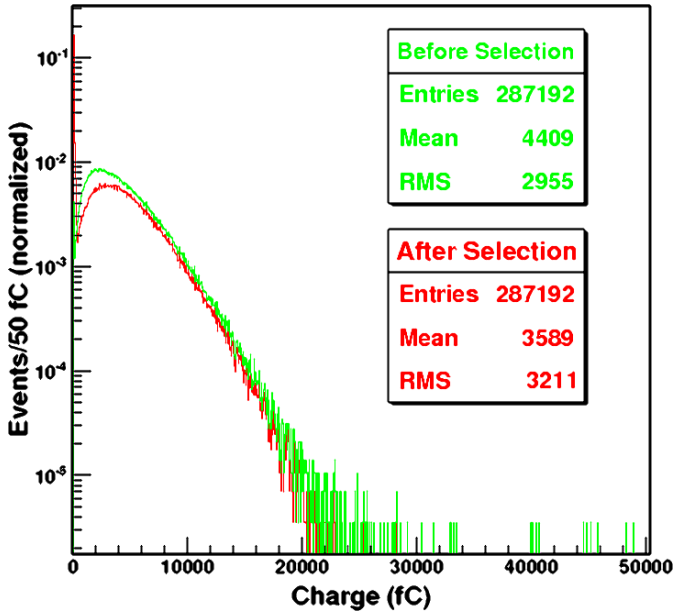

Figure 16: The result of the application of selection and signal recovery algorithm to HF fiber bundle when the PMTs were in the beamline.

6 Conclusions

In the search for a new photomultiplier tube for the CMS forward hadron calorimeter, candidate PMTs with different specifications were tested. The response of PMTs to relativistic charged particles traversing their windows at different incidence orientations was tested with 150 GeV/c muon beam. The HF calorimeter signal was also

mimicked with two test setups in 80 GeV/c electron beam in order to compare PMT performances: around 1 cm-diameter bundle of HF quartz fibers and a 20 cm x 20 cm x 45 cm steel rod calorimeter with quartz fibers placed in between and alongside the rods. The fiber bundle was split into two at one end enabling two readout channels simultaneously. The difference between these two ends in terms of signal quality due to fiber mixing, slight variations in light guide conditions, etc. is negligible.

At front incidence of muons on the PMT windows, the candidate PMTs exhibit significantly better performance with their reduced response magnitude and spread, and PMT window event rates. The miniPMT produces the lowest response to traversing particles since it has the thinnest window among all PMTs under study. It is clearly observed that PMTs with the same type of photocathode - hence same quantum efficiency - and gain have identical responses.

Side muon incidence response is higher and has a wider spectrum when compared to front incidence response. This is due to the difference in the distance traveled by muons inside the PMT window. Measurements with various angles of muon incidence also prove that the response becomes larger as the angle between the PMT window and the beam direction is decreased.

Fiber bundle data was first filtered for exact fiber location utilizing one of the wire chambers in the beamline. Therefore, the response solely by the Čerenkov radiation in the fibers was measured. Measurements show that the candidate PMTs have superior performance over the HFPMT on detection of Čerenkov light as expected from their proposed quantum efficiencies. It is also concluded that the four anode and single anode PMTs that have the same kind of photocathode material have identical responses.

Fiber calorimeter study is performed by reading out a single PMT response from the back of the calorimeter where the quartz fibers are bundled to form a single tower. The single anode and four anode PMTs show significantly improved responses compared to the HFPMT. The miniPMT does not constitute a strong competitor for the other types of PMTs as more than one miniPMT would be required to read out the fiber bundle in the HF calorimeter towers.

For the four anode PMT, an effective and simple algorithm for selecting PMT window events and recovering the signal from the quadrants that do not show PMT window event signature is presented and implemented on front and side muon incidence data as well as the fiber bundle data. This simple method proves to be an effective way of selecting PMT window events and recovering the signal with available information. The method can be utilized both for refining detector measurements and for the elimination of cosmic interference online or offline.

Acknowledgements

This project was carried out with financial support from U.S. Department of Energy, U.S. National Science Foundation, RMKI-KFKI (Hungary), Russian Ministry of Education and Science, Russian State Committee for Atomic Energy, Scientific and Technical Research Council of Turkey (TUBITAK), Turkish Atomic Energy Agency (TAEK) and Bogazici University Research Fund.

References

[1] S. Chatrchyan et al. (CMS Collabration), "The CMS Experiment at the CERN LHC," JINST 3, S08004, pp. 145-149 (2008).

[2] CMS Collaboration, "CMS Physics TDR: Volume I, Detector Performance and Software," CERN/LHCC 2006-001 (2006).

[3] S. Abdullin et al. (CMS Collaboration), "Design, Performance, and Calibration of CMS Forward Calorimeter Wedges," Eur. Phys. J. C 53, 1 (2008).

[4] http://www.hamamatsu.com/.

[5] U. Akgun et al., "Complete Tests of 2000 Hamamatsu R7525HA Phototubes For The CMS-HF Forward Calorimeter," Nucl. Instrum. Meth. A550 (2005) 145-156; U. Akgun et al., "Comparison of PMTs From Three Different Manufacturers For The CMS-HF Forward Calorimeter," IEEE Trans. Nucl. Sci. 51 (2004) 1909-1915; U. Akgun et al., "Afterpulse Timing and Rate Investigation of Three Different Hamamatsu Photomultiplier Tubes," JINST 3 T01001 (2008).

[6] http://ab-div-atb-ea.web.cern.ch/ab-div-atb-ea/BeamsAndAreas/resultbeam.asp?beamline=H2.

[7] T. Zimmerman and M. Sarraj, "A Second Generation Charge Integrator and Encoder ASIC," IEEE Trans. Nucl. Sci. 43, 1683 (1996); T. Zimmerman and J.R. Hoff, "The Design of a Charge-Integrating Modified Floating-Point ADC Chip," IEEE J. Solid State Circuits 39, 895 (2004).

[8] https://twiki.cern.ch/twiki/bin/view/CMS/WorkBookCMSSWFramework.

[9] D. Motta and S. Schonert, "Optical Properties of Bialkali Photocathodes," Nucl. Instrum. Meth. A539, 217 (2005).